PAPER

Cobalt nanoparticle-embedded nitrogen-doped carbon/carbon nanotube frameworks derived from a metal–organic framework for tri-functional ORR, OER and HER electrocatalysis†

Hele Guo, ‡[a] Qichun Feng, ‡[a] Jixin Zhu, [ID][b] Jingsan Xu, [ID][c] Qianqian Li,[a] Siliang Liu,[a] Kaiwen Xu,[a] Chao Zhang [ID] *[a] and Tianxi Liu [ID] *[a]

Developing active and stable electrocatalysts of earth-abundant elements towards the oxygen reduction reaction (ORR), oxygen evolution reaction (OER) and hydrogen evolution reaction (HER) still remains a crucial challenge. Herein, a cobalt-containing metal–organic framework using adenine as a ligand was synthesized and pyrolyzed without any other precursors, forming a cobalt nanoparticle-embedded nitrogen-doped carbon/carbon nanotube framework (Co@N-CNTF). Due to the abundant active sites of homogeneously distributed cobalt nanoparticles within nitrogen-doped graphitic layers, the resultant Co@N-CNTF catalysts exhibit an efficient and stable electrocatalytic performance as a tri-functional catalyst towards the ORR, OER and HER, including a high half-wave potential of 0.81 V *vs.* RHE for the ORR, and a low overpotential at 10 mA cm^{-2} for the OER (0.35 V) and HER (0.22 V). As a proof-of-concept, the Co@N-CNTF as an OER/HER bifunctional catalyst for full water splitting affords an alkaline electrolyzer with 10 mA cm^{-2} under a stable voltage of 1.71 V. Moreover, an integrated unit of a water-splitting electrolyzer using the Co@N-CNTF catalysts, which is powered with a rechargeable Zn–air battery using the Co@N-CNTF as an ORR/OER bifunctional catalyst on air electrodes, can operate under ambient conditions with high cycling stability, demonstrating the viability and efficiency of the self-powered water-splitting system.

[a]State Key Laboratory for Modification of Chemical Fibers and Polymer Materials, College of Materials Science and Engineering, Innovation Center for Textile Science and Technology, Donghua University, Shanghai 201620, P. R. China. E-mail: czhang@dhu.edu.cn; txliu@dhu.edu.cn; txliu@fudan.edu.cn

[b]Shaanxi Institute of Flexible Electronics (SIFE), Northwestern Polytechnical University (NPU), 127 West Youyi Road, Xi'an 710072, P. R. China

[c]School of Chemistry, Physics and Mechanical Engineering, Queensland University of Technology, Brisbane, QLD 4001, Australia

† Electronic supplementary information (ESI) available: SEM images of Co@N-CNTF-1-600, Co@N-CNTF-2-600, Co@N-CNTF-3-600, and Co@N-CNTF-2-800; TEM images and size distributions of Co nanoparticles within Co@N-CNTF-2-600 and Co@N-CNTF-2-800; XPS survey spectra of Co@N-CNTF; Co 2p and N 1s XPS spectra of Co@N-CNTF-2 prepared at different temperatures; N contents in the Co@N-CNTF; contents of various N forms in Co@N-CNTF-2 prepared at different temperatures; XRD patterns and Raman spectra of Co@N-CNTF-2 prepared at different temperatures; LSV curves of Co@N-CNTF-2 prepared at different temperatures; Tafel slopes and CV curves of Co@N-CNTF-1, Co@N-CNTF-2, and Co@N-CNTF-3; CV plots of Co@N-CNTF-2-600, Co@N-CNTF-1, Co@N-CNTF-2, Co@N-CNTF-3, and Co@N-CNTF-2-800 at different scan rates; the capacitive currents plotted as a function of scan rates; XRD pattern and Raman spectra of Co@N-CNTF-2-700 after OER cycling; XPS spectra of Co@N-CNTF-2-700 after OER cycling; ORR performance of Co@N-CNTF-2-700 after OER cycling; schematic of a home-made water splitting device; volume of produced H$_2$ and O$_2$ as a function of time for the water splitting device; summary of ORR and OER activities of Co@N-CNTF-2 with other Co-based bifunctional oxygen electrocatalysts. See DOI: 10.1039/c8ta11400e

‡ These authors contributed equally to this work.

Introduction

There exist an urgent pursuit and global demand for sustainable energy conversion and storage due to severe energy shortages and environmental problems. A reversible conversion between chemical energy and electrical energy is extremely attractive because of its intrinsic environmental friendliness and safety.[1–4] Hydrogen is a safe and reliable energy source with a high calorific value, low density and green conversion products (H$_2$O).[5] The production of hydrogen and oxygen gas through electrolysis of water corresponding to the hydrogen evolution reaction (HER) at the cathode and oxygen evolution reaction (OER) at the anode, respectively, provides an efficient strategy for large-scale production of hydrogen with high energy-conversion efficiency.[6] Besides, the reversible reactions in the oxygen electrodes including the OER and oxygen reduction reaction (ORR) play key roles in determining the performance of rechargeable metal–air batteries and reversible fuel cells.[7] Therefore, it is extremely imperative to develop highly efficient and stable electrocatalysts by reducing overpotentials as well as accelerating the reaction kinetics for the HER, OER and ORR.[8–12]

To date, Pt-based electrocatalysts have shown the highest activity for the HER and ORR while Ru/Ir-based materials are

3664 | *J. Mater. Chem. A*, 2019, 7, 3664–3672

This journal is © The Royal Society of Chemistry 2019

state-of-the-art electrocatalysts for the OER.[13] However, Pt, Ru and Ir have prohibitive costs due to their limited resources, and sluggish activities for the reverse reactions essential for rechargeable metal–air batteries, reversible fuel cells and over-all water-splitting systems.[14] Therefore, the on-going challenge is searching for a non-precious-metal catalyst that can well match the electrocatalytic performance of Pt, Ru and Ir-based materials. Carbon materials (such as graphene, carbon nano-tubes, and porous carbon) have demonstrated promising elec-trocatalytic properties for air cathodes due to their large surface area, high electrical conductivity and good electrochemical stability.[15–17] In particular, nitrogen with a lone pair of electrons doped in carbon materials manifests significantly boosted ORR and OER activity.[15,18] For the HER, N doping can also activate the adjacent carbon by endowing it with an easier access to inter-mediate products of H_2 and hence generating hydrogen with a low overpotential.[19] Therefore, it is very hopeful to develop unique nitrogen-doped (N-doped) carbon materials for achieving the acceleration of the electrocatalytic HER, OER and ORR reactions,[20–22] yet there have been no very heart-stirring results in this regard.

Metal–organic frameworks (MOFs) are essentially novel porous materials with a periodic network by connecting metal clusters with organic linkers. Three inherent attributes are required to define a material as a MOF, namely, strong bonding providing robustness, linking units, and geometrically well-defined crystalline structures. MOFs typically exhibit a low density ($0.2–1$ g cm^{-3}), high surface area ($500–4500$ m^2 g^{-1}) and reasonable thermal/mechanical stability. More importantly, the ability to tune the pore structure and size of MOFs by choosing appropriate building blocks greatly expands their potential applications.[23] In recent years, uniquely nanostructured N-doped carbon materials derived from MOFs have been rationally synthesized, exhibiting a high electrocatalytic activity especially for the ORR and OER.[24–26] MOFs are promising carbon sources due to their easy construction of topologically diverse porous materials with transition-metal clusters and extremely high nitrogen contents in organic linkers. However, the development of MOF-derived N-doped porous carbon materials towards tri-functional electrocatalysis for the ORR, OER and HER is rarely reported.[27–32]

Herein, cobalt nanoparticle-embedded N-doped carbon/carbon nanotube frameworks (Co@N-CNTFs) were prepared by a facile pyrolysis of rationally designed Co-containing MOFs simultaneously as the carbon, nitrogen and cobalt sources. Due to their superior compositional and structural features, the resultant Co@N-CNTF catalysts exhibit highly efficient tri-functional catalytic activities towards the ORR, OER and HER. As a proof-of-concept, a rechargeable Zn–air battery is assem-bled using the resultant Co@N-CNTF electrocatalysts as the cathodes by the combination of ORR/OER bifunctional processes, and meanwhile the OER/HER bifunctional processes for an overall water-splitting electrolyzer were simultaneously investigated. Therefore, high-performance tri-functional elec-trocatalysts thus prepared show huge potential for their prac-tical application in sustainable energy conversion.

Experimental

Synthesis of the Co-Ade-MOF

The Co-Ade-MOF was prepared by a solvothermal method. After the dissolution of cobalt acetate tetrahydrate and adenine (135.1 mg, 1.0 mmol) in 10 mL of DMF under stirring, the solution was transferred into a 15 mL Teflon-lined stainless steel autoclave, sealed and heated at 120 °C for 12 h. After cooling, the sediments were washed with ethanol and DI water three times, filtered and dried at 50 °C overnight in a vacuum. Co-Ade-MOF-1, Co-Ade-MOF-2 and Co-Ade-MOF-3 represent the products with the cobalt/adenine molar ratios of 1/6, 1/3 and 1/2, respectively.

Synthesis of the Co@N-CNTF

The Co@N-CNTF catalysts were prepared by the pyrolysis of the Co-Ade-MOFs at a designed temperature under a N_2 flow. After cooling, the products were washed with 1 M HCl and DI water in sequence, and dried at 60 °C overnight. The resulting products are designated as Co@N-CNTF-1-x, Co@N-CNTF-2-x and Co@N-CNTF-3-x, respectively, using Co-Ade-MOF-1, Co-Ade-MOF-2 and Co-Ade-MOF-3 as the precursors, where x represents the pyrolysis temperature.

Electrochemical measurements

The catalytic activities of all the catalysts for the HER, ORR and OER performance were investigated with a CHI 660D electro-chemical workstation in a standard three-electrode system using an Ag/AgCl electrode as the reference electrode, a graphite rod as the counter electrode, and a rotating disk electrode coated with the catalysts as the working electrode. The catalyst ink was prepared by dispersing 5 mg of the samples into 350 μL ethanol and 95 μL Nafion solution (5 wt%). After sonication for 5 min, 5 μL of the catalyst ink was deposited onto a 5 mm diameter polished glassy carbon electrode (Gamry Instruments, Inc.) with a mass loading of ~0.28 mg cm^{-2} and dried at room temperature. For comparison, Pt/C was used as a reference for the ORR and HER, while IrO_2 was used as a reference for the OER.

ORR. A 0.1 M KOH solution bubbled with oxygen was used as the electrolyte. The LSV curves were recorded at different rota-tion speeds of 800, 1200, 1600, 2000 and 2400 rpm at a scan rate of 10 mV s^{-1}. The durability was obtained by recording the chronoamperometry (i–t) curve at 0.66 V $vs.$ RHE at 1600 rpm.

OER. A 1 M KOH solution bubbled with oxygen was used as the electrolyte. The LSV curves were recorded at 1600 rpm at a scan rate of 5 mV s^{-1}. The durability was obtained by recording the chronoamperometry (i–t) curve at the potential with a current density of 10 mA cm^{-2} at 1600 rpm.

HER. A 0.5 M H_2SO_4 and 1 M KOH solution bubbled with N_2 was used as the electrolyte. The LSV curves were recorded at a scan rate of 5 mV s^{-1}. All the potentials in this study were iR corrected and converted to the RHE scale using the Nernst equation ($E_{RHE} = E_{Ag/AgCl} + 0.197 + 0.059$ pH).

Zn–air batteries and water splitting. Zn–air batteries in a two-electrode configuration were assembled according to the

This journal is © The Royal Society of Chemistry 2019

J. Mater. Chem. A, 2019, 7, 3664–3672 | 3665

following procedure. The air electrode was prepared by spraying the catalyst onto a carbon cloth substrate with a loading of 1 mg cm^{-2}. A polished Zn plate (thickness: 1.0 mm, Shengshida Metal Mater. Co. Ltd., China) was applied as the anode, and a 6 M KOH solution with 0.2 M zinc acetate was used as the electrolyte. The discharge polarization and power density plots were recorded using a galvanodynamic method. The cycling performance was investigated by conducting galvanostatic discharge–charge measurements at a current density of 10 mA cm^{-2} in ambient air (1200 s discharging followed by 1200 s charging). The durability performance toward overall water splitting was evaluated by using Co@N-CNTF-2-700 as the catalyst for both OER and HER in a two-electrode device in 1 M KOH at a current density of 10 mA cm^{-2}. The gas quantification for the overall water splitting was performed by drainage collection processes. Two pieces of carbon cloth loaded with Co@N-CNTF-2-700 catalysts were placed in a sealed H-typed tube filled with 1 M KOH electrolyte. A chronopotentiometry operation with a constant current density of 10 mA cm^{-2} was applied to produce H$_2$ and O$_2$ gases, which were then collected and calibrated using graduated cylinders.

Results and discussion

The preparation of the Co@N-CNTF consists of two steps including the synthesis of cobalt-containing biological MOFs (bio-MOFs) with a tunable cobalt/ligand ratio followed by the pyrolysis of the as-obtained MOF samples in a N$_2$ flow. Bio-MOFs not only have the advantages of large porosity and diversity similar to conventional MOFs, but also have scarce toxicity and good biocompatibility for practical applications. Adenine is a green and cheap biomolecule as a unique carbon and nitrogen source due to the following reasons: (1) adenine contains a variety of coordination modes, and can easily construct a topologically diverse family of MOF-based materials; (2) the molecular structure of adenine is rigid enough and favourable to form permanently porous materials; (3) the N content (51.8%) within adenine and its pyrolysis products is extremely high.[33] Cobalt-containing bio-MOFs were synthesized using cobalt acetate and adenine as the cobalt source and ligand, respectively, with a tunable feeding cobalt/ligand ratio. Co-Ade-MOF-1, Co-Ade-MOF-2 and Co-Ade-MOF-3 represent the products with the cobalt/adenine molar ratios of 1/6, 1/3 and 1/2, respectively. Fig. 1a exhibits the ball-and-stick model of the Co-Ade-MOFs showing the crystallographic structure of the as-obtained MOFs based on a standard Crystallographic Information File (CIF) from the view of the c-axis direction. Subunits composed of two cobalt ions, two adeninate and two acetates are bridged by the coordination bonds assembled into three-dimensional (3D) networks. X-ray diffraction (XRD) patterns of the as-obtained Co-Ade-MOFs are in high agreement with the corresponding framework structures and simulated Co-Adenine MOFs from the single-crystal data (Fig. 1b).[33] In addition, the intensity of the XRD patterns obviously increases with the increased cobalt contents within these Co-Ade-MOFs, indicating the different sizes and crystallinity degrees of the Co-Ade-MOFs (Fig. 1b).[34,35] Compared with the neat ligand adenine, the
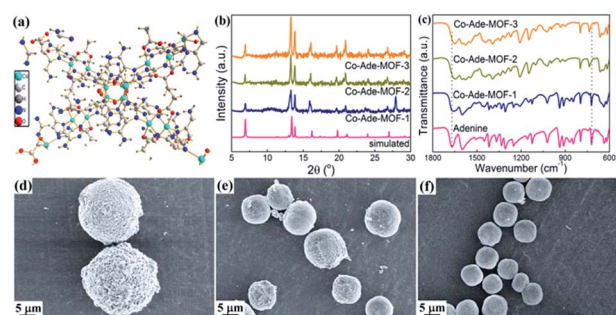

Fig. 1 (a) Chemical structure of the Co-Adenine MOF. (b) XRD patterns of the simulated Co-Ade-MOF and the Co-Ade-MOFs with various metal/ligand ratios. (c) FTIR spectra of the adenine and Co-Ade-MOFs. SEM images of (d) Co-Ade-MOF-1, (e) Co-Ade-MOF-2 and (f) Co-Ade-MOF-3.

Fourier transform infrared (FTIR) spectra of the Co-Ade-MOFs (Fig. 1c) clearly show the emergence of the Co–N stretching vibrations at ~1210 cm^{-1} and the red shift of the C–N at ~1750 cm^{-1}, indicating the formation of strong coordination bonds between the cobalt ions and ligands.[36] The low-intensity peaks in the range of 600–800 cm^{-1} are attributed to the Co=O stretching vibrations.[37] The field emission scanning electron microscopy (FESEM) images of the as-obtained Co-Ade-MOFs (Fig. 1d–f) indicate that the particle sizes of the MOFs gradually decrease when increasing the cobalt content within the MOFs as more metal ions within the framework would induce enhanced metal–ligand coordination interactions and thus decrease the MOF particle size.[38]

Second, the Co-Ade-MOFs were pyrolyzed at a designed temperature under the protection of nitrogen. Co@N-CNTF-1, Co@N-CNTF-2 and Co@N-CNTF-3 represent the products pyrolyzed at 700 °C from the Co-Ade-MOF-1, Co-Ade-MOF-2 and Co-Ade-MOF-3 precursors, respectively. Upon the pyrolysis at 700 °C, clusters with a diameter of ~250 nm were observed with densely grown CNTs in Co@N-CNTF-1 (Fig. 2a, b) and Co@N-CNTF-2 (Fig. 2c, d), while Co@N-CNTF-3 (Fig. 2e, f) maintains the initial spherical shape of Co-Ade-MOF-3 but with densely grown CNTs on the particle surface. Co@N-CNTF-2 was then characterized using a transmission electron microscope (TEM) to further investigate its detailed structure. In Co@N-CNTF-2, the clusters from the SEM observations are composed of plenty of CNTs entangled with each other, and the cobalt nano-particles embedded in few-layer graphitic carbon layers are homogeneously dispersed within the CNT framework (Fig. 3a, b). A high-magnification TEM image further shows that these cobalt nanoparticles with an average size of 11.1 nm (inset of Fig. 3c) are encapsulated in few-layer graphitic carbon layers, which are a part of a bamboo shaped CNT due to nitrogen doping (Fig. 3c). The lattice fringes of the sidewalls of CNTs and cobalt nanoparticles are measured to be 0.34 and 0.21 nm (Fig. 3d), respectively, which match well with the d-spacing of the (002) plane of CNTs and the (111) plane of metallic cobalt, respectively. In addition, amorphous carbon is also observed within the framework. From the HADDF-TEM image and corresponding elemental mappings of Co@N-CNTF-2 (Fig. 3e),
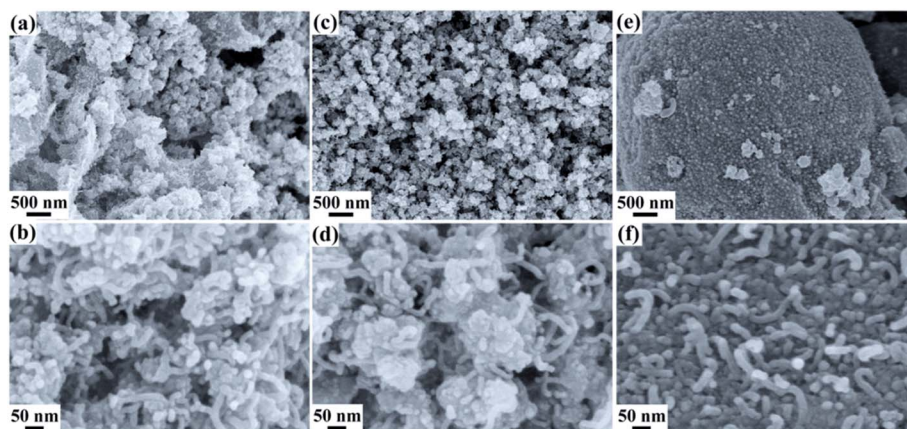
Fig. 2 SEM images of (a and b) Co@N-CNTF-1, (c and d) Co@N-CNTF-2 and (e and f) Co@N-CNTF-3 at low and high magnifications, respectively.

carbon, nitrogen and oxygen elements are observed to be dispersed homogeneously within Co@N-CNTF-2, while the spherical shape of the cobalt element clearly indicates the nanoparticle morphology of the embedded cobalt within Co@N-CNTF-2. To be specially noted, the nitrogen and cobalt contents are measured to be 6.5% and 5.8%, respectively within the sample surface. Therefore, the straightforward strategy for the pyrolysis preparation of the Co@N-CNTF is extremely simple and efficient enabling a large-scale production of such cobalt nanoparticle-embedded N-doped carbon structures.

The morphological evolutions from the Co-Ade-MOFs to Co@N-CNTFs were then monitored by observing the FESEM images of the Co-Ade-MOFs at a low pyrolysis temperature of 600 °C (Fig. S1†). Upon the pyrolysis, Co-Ade-MOF-1 and Co-Ade-MOF-2 fragmentize into tiny spheres while Co-Ade-MOF-3 still maintains its original spherical shape, indicating that higher contents of cobalt ions within the MOFs favour the thermal and structural stability. TEM images show that the

formed cobalt nanoparticles with a mean size of 9.2 nm are uniformly distributed within the carbon matrix (Fig. S2a–c†). By comparing the morphological evolutions between the MOF samples pyrolyzed at 600 and 700 °C, the possible formation mechanism for *in situ* growing CNTs could be derived. During the heating process between 600 and 700 °C, the organic precursors containing carbon and nitrogen would violently decompose into organic vapor, which could be easily trapped by the embedded cobalt nanoparticles and catalyzed for the growth of N-doped CNTs. As a result, the CNT framework forms tightly fitting the shape of the fragmentized tiny spheres. As the cobalt contents increase for Co-Ade-MOF-3, shorter CNTs were catalyzed because of limited carbon sources relative to abundant cobalt nanoparticles. In addition, direct pyrolysis of Co-Ade-MOF-2 at a temperature of 800 °C was conducted. The SEM and TEM images of Co@N-CNTF-2-800 (Fig. S3a–b, S4a–c†) indicate the formation of CNTs with relatively larger diameters because of the *in situ* formed larger cobalt nanoparticles
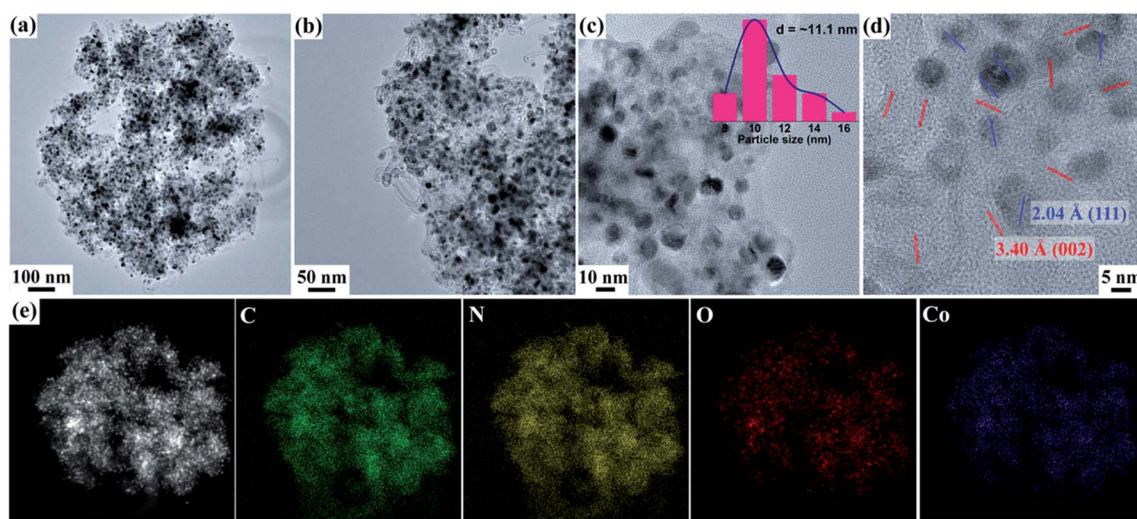

Fig. 3 (a–c) TEM and (d) high-resolution TEM images of Co@N-CNTF-2, and the inset of (c) is corresponding size distributions of embedded Co nanoparticles. (e) HAADF-TEM and corresponding EDX elemental mappings of C, N, O and Co in Co@N-CNTF-2, respectively.

(~13.8 nm) at the higher temperature, which would catalyse the growth of CNTs with larger outer diameters.

X-ray photoelectron spectroscopy (XPS) is applied to probe the surface elemental and bonding configurations of the Co@N-CNTF. The peaks ascribed to carbon, nitrogen and cobalt can be observed from the XPS survey spectra. Although the intensity of the carbon signal is very high, the fine scan for cobalt and nitrogen is still clear (Fig. S5†). The contents of the nitrogen species in the Co@N-CNTF samples are calculated to be 23 to 6.2 at% (Fig. S6†). The high-resolution Co 2p and N 1s peaks were primarily employed to determine the bonding configurations of the Co and N atoms in the Co@N-CNTF samples, respectively. The peaks observed at 793.6 and 778.2 eV correspond to the Co $2p_{1/2}$ states and Co $2p_{3/2}$ binding energy, respectively, which match well with the metallic cobalt (Fig. 4a and S7a†). The presence of two peaks at 780.6 and 795.7 eV suggests that Co is mainly in the oxidized state and the interactions between cobalt nanoparticles and N-doped CNTs, and the other two peaks at 786.0 and 803.5 eV are satellite peaks.[39] Similarly, the deconvolution peaks of N 1s at 398.4, 400.1 and 401.1 eV correspond to pyridinic-N, pyrrolic-N and graphitic-N, respectively (Fig. 4b and S7b†). Fig. 4c and S8† show that the graphitic-N and pyridine-N within the N contents of Co@N-CNTF-2 are ~90%. This increment of doped N heteroatoms is attributed to the enrichment of carbon defects, as confirmed by Raman spectra. The two main peaks at 1350 and 1580 cm^{-1} belong to the D band and G band, respectively, where the D band indicates disordered carbon and the G band is typical of in-plane vibrations of sp^2 carbon. The specific value of the relative intensity between the D band and G band (I_D/I_G) indicates the degree of disordered carbon structure.[40] Fig. S9† indicates that the value of I_D/I_G decreases gradually, demonstrating that higher pyrolysis temperature could produce carbon-based materials with higher degrees of graphitization. Fig. 4d shows that the value of I_D/I_G of Co@N-CNTF-1 is 1.05, which is higher than those of Co@N-CNTF-2 (1.00) and Co@N-CNTF-3 (0.96). Therefore, the Co@N-CNTF-2 and Co@N-CNTF-3 catalysts with higher cobalt/ligand ratios have fewer defects and a relatively complete graphitic structure.[14] The as-prepared Co@N-CNTF was also confirmed by X-ray diffraction (XRD)

measurements. The diffraction pattern at $2\theta = 23.1°$ is assigned to the (002) diffraction plane of carbon for the Co@N-CNTF (Fig. 4e). Moreover, there are several additional peaks at $2\theta = 44.2°$ and $51.5°$, which are attributed to the (111) and (200) crystal planes of metallic Co (JCPDS no. 15-0806), respectively. However, no significant crystalline patterns of metallic Co are observed in Co@N-CNTF-2-600, and stronger patterns are found in Co@N-CNTF-2-800 (Fig. S10†). The large surface area and optimized pore size distributions of the nanostructured catalysts would be beneficial for subsequent electrochemical processes demanding efficient ion diffusions. Fig. 4f clearly indicates that the specific surface areas are calculated as 276.2, 214.3, and 209.7 cm^2 g^{-1} for Co@N-CNTF-1, Co@N-CNTF-2 and Co@N-CNTF-3, respectively. The pore sizes of the Co@N-CNTF are approximately 0.5–4 nm, which are favorable for the effective transport of both aqueous electrolyte ions and gaseous species.[41]

In contrast to the traditional view that transition-metal nanoparticles embedded in few-layer graphitic shells would be electrocatalytically inert, the uniquely structured metal@few-layer graphitic layer shows higher activities toward electrocatalytic reactions including the ORR, OER and HER. On one hand, the metal nanoparticles not only catalyze the formation of hollow carbon structures such as carbon nanotubes and onions, which could improve the electrical conductivity of the whole hybrid structures.[42] On the other hand, the few-layer graphitic shells could prevent the embedded metal nanoparticles from acid corrosion, oxidation and aggregation during the electrocatalytic processes especially at high oxidation potentials in high acidic electrolytes, resulting in excellent durability and stability in tough environments.[43] Moreover, the cobalt nanoparticle@N-doped carbon core–shell architecture provides an effective pathway to tailor the electronic structure of the catalyst, and thereby greatly decreases the adsorption free energy and local work function, which would promote the adsorption and desorption of reaction intermediates.[13]

The ORR performance of the Co@N-CNTF was evaluated by cyclic voltammetry (CV) measurements in a 0.1 M KOH electrolyte. Fig. 5a displays the CV curves of the Co@N-CNTF electrodes in N$_2$- and O$_2$-saturated electrolytes, respectively. No obvious redox peaks can be identified from the CV curves of the three electrodes in the N$_2$-saturated electrolyte. In contrast, well-defined oxygen reduction peaks arise in the O$_2$-saturated electrolyte, suggesting a high intrinsic ORR catalytic activity for the Co@N-CNTF catalysts. The ORR catalytic performance of the Co@N-CNTF catalysts is further compared with that of commercial Pt/C. Fig. 5b and S11† show the linear sweep voltammetry (LSV) curves of the Co@N-CNTF as well as Pt/C catalysts. Among the Co@N-CNTF catalysts, the Co@N-CNTF-2 shows a superior ORR catalytic performance with higher onset (0.91 V) and half-wave potentials (0.81 V) than those of Co@N-CNTF-1, Co@N-CNTF-3, Co@N-CNTF-2-600 and Co@N-CNTF-2-800 (onset potentials defined as the potential corresponding to a current density of -0.10 mA cm^{-2}), and only ~30 mV more negative half-wave potential than that of commercial Pt/C (0.84 V). The electron transfer number (n) for the ORR was calculated from the LSV curves at various rotation rates (800–2400 rpm)
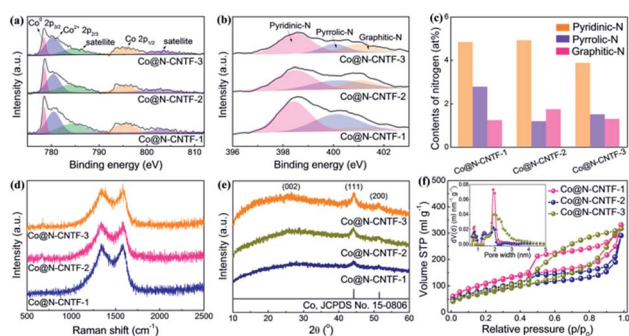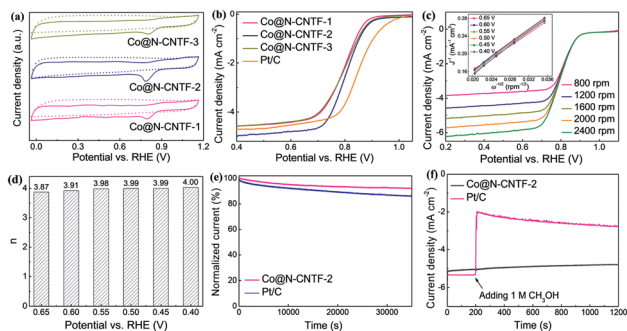

Fig. 4 (a) Co 2p and (b) N 1s XPS spectra of the Co@N-CNTF. (c) Atomic nitrogen contents in terms of different nitrogen forms of the Co@N-CNTF. (d) Raman spectra, (e) XRD patterns and (f) nitrogen sorption/desorption isotherms of the Co@N-CNTF. The inset of (f) is the corresponding pore size distributions of the Co@N-CNTF.

3668 | J. Mater. Chem. A, 2019, 7, 3664–3672

This journal is © The Royal Society of Chemistry 2019

Fig. 5 (a) CV curves of the Co@N-CNTF in N_2- (imaginary line) and O_2-saturated (full line) 0.1 M KOH with a sweep rate of 50 mV s^{-1}. (b) LSV curves of the Co@N-CNTF and Pt/C at 1600 rpm. (c) LSV curves of Co@N-CNTF-2 at various rotation speeds, inset: K–L plots of the catalysts at various potentials. (d) Electron transfer number of Co@N-CNTF-2 at various potentials based on the K–L plots. (e) Chronoamperometric responses of Co@N-CNTF-2 and Pt/C at 0.66 V vs. RHE in O_2-saturated 0.1 M KOH at 1600 rpm. (f) Methanol tolerance evaluation of Co@N-CNTF-2 and Pt/C with the addition of 1 M methanol.

and potentials (0.40–0.65 V) by using the Koutecky–Levich (K–L) equation. The K–L plots from LSV curves are given in the inset of Fig. 5c, which exhibits a good linearity for potentials from 0.40 to 0.65 V with a value of 3.96 for average electron transfer (n) (Fig. 5d), confirming a four-electron oxygen reduction process for the catalytic oxygen reduction.[44,45] The Tafel slope of Co@N-CNTF-2 (47.6 mV dec^{-1}) is smaller than those of Co@N-CNTF-1 (49.9 mV dec^{-1}) and Co@N-CNTF-2 (57.1 mV dec^{-1}), demonstrating that the Co@N-CNTF-2 catalyst has a fast electron transfer rate (Fig. S12†). Furthermore, to investigate the intrinsic electrocatalytic activity in detail, the electrochemical double-layer capacitances (C_{dl}) of the Co@N-CNTF catalysts were calculated based on CV curves at different scan rates. Co@N-CNTF-2 manifests the highest C_{dl} of 10.0 mF cm^{-2}, which is much higher than that of Co@N-CNTF-2-600 (1.8 mF cm^{-2}), Co@N-CNTF-1 (9.5 mF cm^{-2}), Co@N-CNTF-3 (4.9 mF cm^{-2}) and Co@N-CNTF-2-800 (6.8 mF cm^{-2}), confirming the highest electrochemical surface area of the Co@N-CNTF-2 catalyst for the ORR (Fig. S13†).

The Co@N-CNTF-2 catalyst has excellent stability for the ORR, as demonstrated by the chronoamperometric test (Fig. 5e). About 92.3% of the current retention is observed for Co@N-CNTF-2, whereas the Pt/C catalyst manifests a much lower current retention of 86.1% after the chronoamperometric process for 35 000 s. Besides, the methanol crossover effect for the evaluation of such catalysts for practical application was also tested. The chronoamperometric responses of the Co@N-CNTF-2 and Pt/C catalysts were recorded at a rotation rate of 1600 rpm in Fig. 5f. The current density of Co@N-CNTF-2 is ~5.2 mA cm^{-2} and no obvious disturbance is observed when methanol is added at 200 s. In contrast, Pt/C exhibits an immediately sharp current jump because of the initiation of methanol oxidation reactions. The superior durability of the Co@N-CNTF-2 catalyst is ascribed to the efficient protection of Co nanocrystals by few-layer graphitic shells.[39] In general, the

Co@N-CNTF-2 catalyst possesses good long-term stability and excellent tolerance to methanol over Pt/C in alkaline media.

The bifunctional performance of the Co@N-CNTF catalysts towards the OER and HER was investigated in detail. Fig. S14† depicts the CV curves of the Co@N-CNTF catalysts. For all Co@N-CNTF catalysts, the current densities for these electrodes increase suddenly in the potential range of 1.47 to 1.70 V, indicating their apparent OER catalytic activity. Fig. 6a indicates that the potential required to reach the current density of 10 mA cm^{-2} using the Co@N-CNTF-2 catalyst is 1.58 V vs. RHE. This potential is slightly lower than those of Co@N-CNTF-1 (1.65 V) and Co@N-CNTF-3 (1.64 V). The Tafel slopes of these catalysts are also calculated (Fig. 6b) in order to investigate the OER reaction kinetics of these catalysts. The Tafel slope of Co@N-CNTF-2 (61.4 mV dec^{-1}) is significantly lower than that of Co@N-CNTF-1 (113.5 mV dec^{-1}) and Co@N-CNTF-3 (102.3 mV dec^{-1}). The lower Tafel slope of Co@N-CNTF-2 indicates that the catalyst possesses a faster OER catalytic kinetics. Co@N-CNTF-2 also shows excellent OER stability, where negligible catalytic degradation is observed when recording the chronoamperometry (i–t) curve at the potential with a current density of 10 mA cm^{-2} at 1600 rpm for 50 000 s (Fig. 6c), which could be attributed to the hierarchical pore structure with more exposed active sites, good conductivity for efficient electron transfer and unique nanostructures of Co nanoparticles wrapped in N-doped carbon shells. The overvoltage of the ORR and OER ($\Delta E = E_{j=10} - E_{1/2}$) represents efficiency loss, which is considered as the key parameter to evaluate the bifunctional electrocatalytic activity of catalysts.[41,46,47] The smaller ΔE value manifests the better ability of a catalyst working as a reversible oxygen electrode. Co@N-CNTF-2 exhibits an outstanding activity of 0.77 V as an overall oxygen electrode, which is much better than those of Co@N-CNTF-1 (0.86 V) and Co@N-CNTF-3 (0.85 V) (Fig. 6d). Table S1† compares our Co@N-CNTF catalyst with other Co-based bifunctional oxygen catalysts in the literature, indicating that the Co@N-CNTF-2 catalyst is a promising bifunctional catalyst for both ORR and OER. To further inspect the surface-evolution process of such a Co@N-CNTF-2 catalyst in 1 M KOH, we collected and characterized the as-obtained catalyst after OER cycling for 50 000 s. Fig. S15† shows the XRD pattern of Co@N-CNTF-2 corresponding to metallic Co (JCPDS no. 15-0806) upon cycling, indicating that the cobalt nanoparticles embedded in N-doped carbon shells have good chemical stability. According to Raman spectra (Fig. S16†), after the OER testing, the intensity ratio of I_D/I_G slightly increases to 1.04, which is mainly attributed to slight corrosion of surface carbon structures at high operating voltages for the OER. Fig. S17a† shows the XPS survey spectra of Co@N-CNTF-2 after cycling for the OER. The O 1s XPS peaks, which can be deconvoluted into four peaks, attributed to Co–O (530.8 eV), OH^- (532.3 eV), H_2O_{ads} (533.9 eV) and C–O species (535.7 eV), significantly increase upon cycling. Fig. S17c† shows that a portion of Co^{2+} in Co@N-CNTF-2 converts into Co^{3+} after continuous generation of oxygen. Moreover, C 1s XPS spectra can be deconvoluted into four peaks consisting of C–C at 284.6 eV, C=C at 285.4 eV, C–O at 286.7 eV, and C=O at 288.1 eV, respectively. After cycling for the OER, the
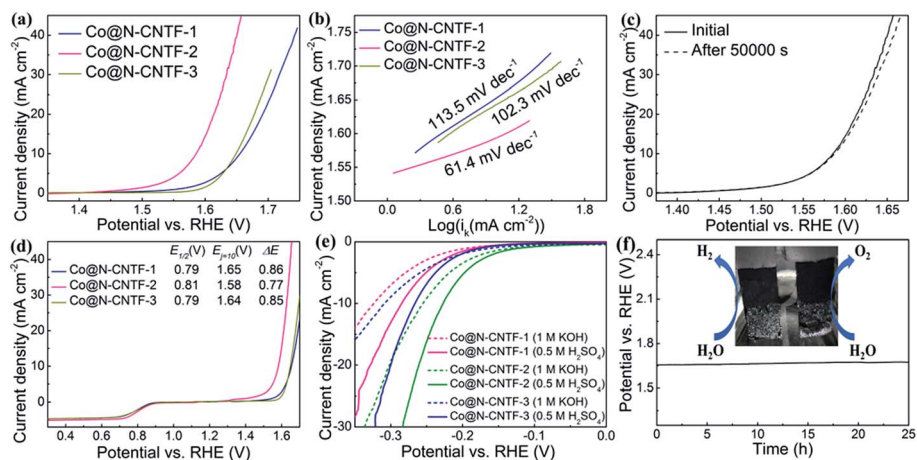
This journal is © The Royal Society of Chemistry 2019

J. Mater. Chem. A, 2019, 7, 3664–3672 | 3669

Fig. 6 (a) LSV curves of the Co@N-CNTF at 5 mV s^{-1}. (b) Tafel slopes of the Co@N-CNTF. (c) LSV curves of Co@N-CNTF-2 after the durability test at 10 mA cm^{-2}. (d) ORR and OER polarization curves of the Co@N-CNTF with a positive scan at 1600 rpm. (e) HER polarization curves of the Co@N-CNTF in N$_2$-saturated 1 M KOH and 0.5 M H$_2$SO$_4$, respectively, at 5 mV s^{-1}. (f) Chronoamperometric responses of Co@N-CNTF-2//Co@N-CNTF-2 in a two-electrode system for water splitting at a current density of 10 mA cm^{-2}. Inset of (f) is a photograph of the electrocatalytic evolution of H$_2$ (right) and O$_2$ (left) bubbles.

relative intensities of C–O and C=O slightly increase (Fig. S17d†), which is ascribed to slight oxidation of the carbon shell at high OER potentials.[48] To examine the effect of continuous OER testing on the ORR performance, the LSV curve of the Co@N-CNTF-2 catalyst for the ORR side after cycling for the OER is shown in Fig. S18,† in which the half-wave potential has only a small negative shift of 10 mV. In the HER half-reaction in Fig. 6e, the Co@N-CNTF-2 catalyst exhibits an optimum activity with a potential of −260 mV and −226 mV in base and acid electrolytes, respectively, under a current density of 10 mA cm^{-2}. The high contents of pyridinic-N of the Co@N-CNTF-2 surpass those of the Co@N-CNTF-1 and Co@N-CNTF-3 catalysts. In detail, the pyridinic-N could activate adjacent carbon atoms with much improved accessibility of H* and thus accelerate the formation of H$_2$. Since Co@N-CNTF-2 has been proved to be an efficient and stable bifunctional catalyst for both OER and HER, overall water splitting was carried out in a 1 M KOH solution. Co@N-CNTF-2 was loaded on two pieces of carbon cloth to assemble an electrolyzer device. Continuous gas bubbles were observed at both the anode and cathode during the chronoamperometric measurement (inset of Fig. 6f), and the voltage has an inconspicuous change at a current density of 10 mA cm^{-2} after cycling for 25 h (Fig. 6f). The home-made water splitting device using the carbon cloth-loaded Co@N-CNTF-2 catalyst as both cathode and anode was assembled and is shown in Fig. S19a.† The generated H$_2$ and O$_2$ can be collected *via* drainage methods. Fig. S19b† shows that the volume of generated H$_2$ and O$_2$ is approximately equal to the theoretical values under a constant current density of 10 mA cm^{-2}, and the volume ratio of the H$_2$ and O$_2$ is calculated to be approximately 2 : 1. Moreover, the faradaic efficiency of this overall water splitting system is demonstrated to be approaching 100%. The result certifies that Co@N-CNTF-2//Co@N-CNTF-2 as both the cathode and anode can retain a satisfactory stability in a long-period water electrolysis.

Based on the superior ORR, OER, and HER electrocatalytic activity of Co@N-CNTF-2, a self-powered electrochemical overall water splitting system is subsequently demonstrated. The system is powered by two rechargeable Zn–air batteries in series, using the tri-functional Co@N-CNTF-2 catalyst as the air cathode. Meanwhile, Co@N-CNTF-2 is loaded on two pieces of carbon cloth, which are responsible for OER and HER catalytic activity, respectively, during the water electrolysis process. Fig. 7a shows a schematic of the two-electrode rechargeable Zn–air battery. The Co@N-CNTF-2 catalyst was employed as the air cathode to assemble two rechargeable Zn–air batteries in series, which can light up a light-emitting diode (LED) bulb easily (Fig. 7b). The polarization and power density curves of this rechargeable Zn–air battery are shown in Fig. 7c. The Zn–air battery presents a high current density of 55.1 and 153.3 mA cm^{-2} at potentials of 1.0 and 0.5 V, respectively. The maximum power density is as high as 91 mW cm^{-2}, extremely close to that of the battery based on the Pt/C cathode (94 mW cm^{-2}).[45] Fig. 7d reveals the charge and discharge polarization curves of the rechargeable Zn–air batteries employing the Co@N-CNTF-2 catalyst and Pt/C as the air cathode, respectively. The charge and discharge behaviors at high current densities of the Co@N-CNTF-2 cathode exhibit a lower overpotential than that of the Pt/C cathode, further confirming the outstanding catalytic activity of the Co nanoparticles embedded in N-doped graphitic shells.[47,49] The efficiency and long-term rechargeability of Co@N-CNTF-2 and Pt/C for the Zn–air batteries are compared in Fig. 7e. The rechargeable Zn–air battery assumes a stable charge–discharge performance at a current density of 10 mA cm^{-2} with ∼2400 s per cycle. The charge–discharge gap of the Co@N-CNTF-2 battery is only 0.86 V, and it remains at 0.93 V after 100 cycles of continuous operation, which is significantly better than that of the Pt/C battery.

In practice, it is significant to develop efficient, stable, and low-cost electrocatalysts to improve the efficiency of electrochemical reactions. To prove the potential application of the
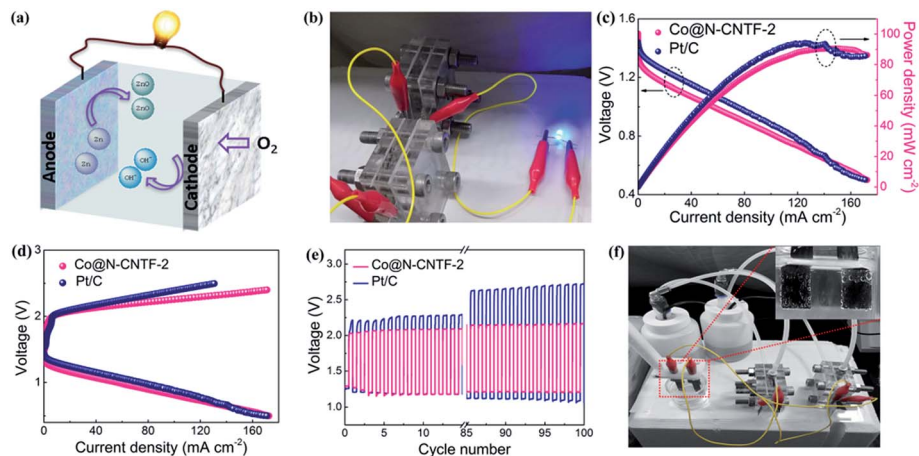
Fig. 7 (a) Schematic illustration of a rechargeable Zn–air battery. (b) A photograph showing an LED light powered by two Zn–air batteries in series. (c) Discharge polarization curve and power density of primary Zn–air batteries using Co@N-CNTF-2 and Pt/C as the air electrode, respectively. (d) Charge and discharge curves of a rechargeable Zn–air battery using Co@N-CNTF-2 and Pt/C as the air electrode, respectively. (e) Cycling stability of rechargeable Zn–air batteries with Co@N-CNTF-2 and Pt/C as the air electrode, respectively. (f) A photograph showing an alkaline water splitting cell powered by two Zn–air batteries in series. Inset of (f) is an enlarged photograph of the electrocatalytic evolution of hydrogen (right) and oxygen (left) bubbles.

Co@N-CNTF-2 catalyst in self-powered water splitting, a water-splitting cell was integrated with rechargeable Zn–air batteries in two series (Fig. 7f). Two pieces of carbon cloth loaded with the Co@N-CNTF-2 catalyst were used as both the cathode and anode towards the evolution of H_2 and O_2, respectively. Significant H_2 and O_2 bubble generation can be observed on these two electrodes (inset of Fig. 7f, and Movie S1†), demonstrating the viability and efficiency of the self-powered water-splitting systems. Due to the appropriate hydrophobicity of the carbon cloth electrodes, bubbles generated during the electrolytic process are easily separated, which favors their long-term stability. Therefore, the tri-functional electrocatalyst based on the non-precious cobalt nanoparticle-embedded carbon nanotube framework possesses great potential for advanced energy devices.

Conclusions

In summary, we developed a facile and low-cost strategy to synthesize Co@N-CNTF catalysts from Co-Ade-MOFs with controllable sizes *via* adjusting the ratio of Co^{2+} and adenine, and pyrolysis temperature under a N_2 atmosphere. Owing to the high pyridine-N content, abundant Co nanoparticles embedded in N-doped graphitic shells and large pore structures, the Co@N-CNTF-2 catalyst shows excellent tri-functional electrocatalysis towards the ORR, OER and HER. The Co@N-CNTF-2 catalyst as an ORR electrocatalyst exhibits a more positive onset potential (0.91 V) and half-wave potential (0.81 V), compared with Co@N-CNTF-1 and Co@N-CNTF-3. The methanol tolerance of Co@N-CNTF-2 was better than that of commercial Pt/C in alkaline media. Co@N-CNTF-2 used as the OER and HER electrocatalyst also reveals a low overpotential, which contributes to its overall water splitting ability. On the other hand, Co@N-CNTF-2 is used as the air electrode for a rechargeable Zn–air battery, which exhibits a low charge/discharge voltage

gap and long-term cycling durability. In addition, the Co@N-CNTF-2//Co@N-CNTF-2 couple maintains excellent stability for 25 h under a current density of 10 mA cm^{-2}. The results indicate that pyrolysis of Co-Ade-MOFs with a controllable particle size can become an economical method towards the preparation of high-performance non-precious metal electrocatalysts for highly efficient rechargeable Zn–air batteries and water splitting.

Conflicts of interest

There are no conflicts to declare.

Acknowledgements

References

1 Z. Peng, S. A. Freunberger, Y. Chen and P. G. Bruce, *Science*, 2012, **337**, 563.

2 M. Wang, Y. Hu, J. Han, R. Guo, H. Xiong and Y. Yin, *J. Mater. Chem. A*, 2015, **3**, 20727.

3 S. Zheng, X. Li, B. Yan, Q. Hu, Y. Xu, X. Xiao, H. Xue and H. Pang, *Adv. Energy Mater.*, 2017, **7**, 1602733.

4 Z. Huang, L. Li, Y. Wang, C. Zhang and T. X. Liu, *Compos. Commun.*, 2018, **8**, 83.

This journal is © The Royal Society of Chemistry 2019

J. Mater. Chem. A, 2019, **7**, 3664–3672 | **3671**

5 A. Serov, M. Padilla, A. J. Roy, P. Atanassov, T. Sakamoto, K. Asazawa and H. Tanaka, *Angew. Chem., Int. Ed.*, 2014, **53**, 10336.

6 W. Tang, Y. Han, C. B. Han, C. Z. Gao, X. Cao and Z. L. Wang, *Adv. Mater.*, 2015, **27**, 272.

7 Z. Cui, G. Fu, Y. Li and J. B. Goodenough, *Angew. Chem., Int. Ed.*, 2017, **56**, 9901.

8 B. Zhu, C. Qu, S. Gao, Z. Liang, H. Zhang and R. Zou, *ChemCatChem*, 2018, **10**, 1113.

9 H. Li, Q. Li, P. Wen, T. B. Williams, S. Adhikari, C. Dun, C. Lu, D. Itanze, L. Jiang, D. L. Carroll, G. L. Donati, P. M. Lundin, Y. Qiu and S. M. Geyer, *Adv. Mater.*, 2018, **30**, 1705796.

10 D. Li, L. Deng, H. Yuan, G. Dong, J. Chen, X. Zhang, Y. Chen and Y. Yuan, *Electrochim. Acta*, 2018, **262**, 297.

11 J. Bai, T. Meng, D. Guo, S. Wang, B. Mao and M. Cao, *ACS Appl. Mater. Interfaces*, 2018, **10**, 1678.

12 H.-X. Zhong, J. Wang, Q. Zhang, F. Meng, D. Bao, T. Liu, X.-Y. Yang, Z.-W. Chang, J.-M. Yan and X.-B. Zhang, *Adv. Sustainable Syst.*, 2017, **1**, 1700020.

13 J. Liu, D. Zhu, C. Guo, A. Vasileff and S.-Z. Qiao, *Adv. Energy Mater.*, 2017, **7**, 1700518.

14 K. Wang, J. Yang, J. Zhu, L. Li, Y. Liu, C. Zhang and T. X. Liu, *J. Mater. Chem. A*, 2017, **5**, 11236.

15 S. Cai, Z. Meng, H. Tang, Y. Wang and P. Tsiakaras, *Appl. Catal., B*, 2017, **217**, 477.

16 B. Ni, C. Ouyang, X. Xu, J. Zhuang and X. Wang, *Adv. Mater.*, 2017, **29**, 1701354.

17 H. Y. Zou, B. W. He, P. Y. Kuang, J. G. Yu and K. Fan, *Adv. Funct. Mater.*, 2018, **28**, 1706917.

18 G. L. Tian, M. Q. Zhao, D. Yu, X. Y. Kong, J. Q. Huang, Q. Zhang and F. Wei, *Small*, 2014, **10**, 2251.

19 M. Fang, G. Dong, R. Wei and J. C. Ho, *Adv. Energy Mater.*, 2017, **7**, 1700559.

20 B. Ni, P. He, W. Liao, S. Chen, L. Gu, Y. Gong, K. Wang, J. Zhuang, L. Song, G. Zhou and X. Wang, *Small*, 2018, **14**, 1703749.

21 Y. Jia, L. Zhang, A. Du, G. Gao, J. Chen, X. Yan, C. L. Brown and X. Yao, *Adv. Mater.*, 2016, **28**, 9532.

22 Y. Tao, X. Xie, W. Lv, D. M. Tang, D. Kong, Z. Huang, H. Nishihara, T. Ishii, B. Li, D. Golberg, F. Kang, T. Kyotani and Q. H. Yang, *Sci. Rep.*, 2013, **3**, 2975.

23 G. Jia, W. Zhang, G. Fan, Z. Li, D. Fu, W. Hao, C. Yuan and Z. Zou, *Angew. Chem., Int. Ed.*, 2017, **56**, 13781.

24 A. Mahmood, W. Guo, H. Tabassum and R. Zou, *Adv. Energy Mater.*, 2016, **6**, 1600423.

25 B. Y. Xia, Y. Yan, N. Li, H. B. Wu, X. W. Lou and X. Wang, *Nat. Energy*, 2016, **1**, 15006.

26 X. Zhao, H. Zhao, T. Zhang, X. Yan, Y. Yuan, H. Zhang, H. Zhao, D. Zhang, G. Zhu and X. Yao, *J. Mater. Chem. A*, 2014, **2**, 11666.

27 T. Meng, Y. N. Hao, L. Zheng and M. Cao, *Nanoscale*, 2018, **10**, 14613.

28 Y. Pan, S. Liu, K. Sun, X. Chen, B. Wang, K. Wu, X. Cao, W. C. Cheong, R. Shen, A. Han, Z. Chen, L. Zheng, J. Luo, Y. Lin, Y. Liu, D. Wang, Q. Peng, Q. Zhang, C. Chen and Y. Li, *Angew. Chem., Int. Ed.*, 2018, **57**, 8614.

29 S. Ghosh and R. N. Basu, *Nanoscale*, 2018, **10**, 11241.

30 Z. Lu, J. Wang, S. Huang, Y. Hou, Y. Li, Y. Zhao, S. Mu, J. Zhang and Y. Zhao, *Nano Energy*, 2017, **42**, 334.

31 C. S. Lim, C. K. Chua, Z. Sofer, K. Klímová, C. Boothroyd and M. Pumera, *J. Mater. Chem. A*, 2015, **3**, 11920.

32 M. Jahan, Z. Liu and K. P. Loh, *Adv. Funct. Mater.*, 2013, **23**, 5363.

33 S. Verma, A. K. Mishra and J. Kumar, *Acc. Chem. Res.*, 2010, **43**, 79.

34 F. K. Shieh, S. C. Wang, S. Y. Leo and K. C. Wu, *Chemistry*, 2013, **19**, 11139.

35 N. Stock and S. Biswas, *Chem. Rev.*, 2012, **112**, 933.

36 W. Hui, B. Li, Y. Du, S. Dong and a. E. Wang, *Chem. Mater.*, 2007, **19**, 2987.

37 M. R. Azhar, P. Vijay, M. O. Tade, H. Sun and S. Wang, *Chemosphere*, 2018, **196**, 105.

38 R. E. Morris and L. Brammer, *Chem. Soc. Rev.*, 2017, **46**, 5444.

39 A. Song, W. Yang, W. Yang, G. Sun, X. Yin, L. Gao, Y. Wang, X. Qin and G. Shao, *ACS Sustainable Chem. Eng.*, 2017, **5**, 3973.

40 J. Zhang, Y. Song, M. Kopec, J. Lee, Z. Wang, S. Liu, J. Yan, R. Yuan, T. Kowalewski, M. R. Bockstaller and K. Matyjaszewski, *J. Am. Chem. Soc.*, 2017, **139**, 12931.

41 X. Yang, K. Li, D. Cheng, W.-L. Pang, J. Lv, X. Chen, H.-Y. Zang, X.-L. Wu, H.-Q. Tan, Y.-H. Wang and Y.-G. Li, *J. Mater. Chem. A*, 2018, **6**, 7762.

42 M. Shen, L.-R. Zheng, W. He, C. Ruan, C. Jiang, K. Ai and L. Lu, *Nano Energy*, 2015, **17**, 120.

43 J. Wang, D. Gao, G. Wang, S. Miao, H. Wu, J. Li and X. Bao, *J. Mater. Chem. A*, 2014, **2**, 20067.

44 S. Chao, G. Wang, D. Xu and Y. Wang, *Int. J. Hydrogen Energy*, 2018, **43**, 11012.

45 Z. Huang, H. Pan, W. Yang, H. Zhou, N. Gao, C. Fu, S. Li, H. Li and Y. Kuang, *ACS Nano*, 2018, **12**, 208.

46 X. Fan, F. Kong, A. Kong, A. Chen, Z. Zhou and Y. Shan, *ACS Appl. Mater. Interfaces*, 2017, **9**, 32840.

47 N. Wang, L. Li, D. Zhao, X. Kang, Z. Tang and S. Chen, *Small*, 2017, **13**, 1701025.

48 K. Fan, H. Zou, Y. Lu, H. Chen, F. Li, J. Liu, L. Sun, L. Tong, M. Toney, M. Sui and J. Yu, *ACS Nano*, 2018, **12**, 12369.

49 Y. Bai, X. Yang, Y. He, J. Zhang, L. Kang, H. Xu, F. Shi, Z. Lei and Z.-H. Liu, *Electrochim. Acta*, 2016, **187**, 543.

3672 | *J. Mater. Chem. A*, 2019, **7**, 3664–3672

This journal is © The Royal Society of Chemistry 2019